Spherical Indexing of Overlap EBSD Patterns for Orientation-related Phases -Application to Titanium

W C Lenthe, L Germain, M R Chini, Nathalie Gey, Marc de Graef

Spherical Indexing of Overlap EBSD Patterns for Orientation-related Phases – Application to Titanium

W.C. Lenthe [a], L. Germain [b,c], M.R. Chini [b], N. Gey [b,c], M. De Graef [a,*]

[a] *Department of Materials Science and Engineering, Carnegie Mellon University, Pittsburgh, PA 15213, USA*

[b] *CNRS, Arts et Métiers ParisTech, LEM3, F-57000 Metz, France*

[c] *Laboratory of Excellence on Design of Alloy Metals for low-mAss Structures (DAMAS), Université de Lorraine, France*

Abstract

We propose a new electron backscatter diffraction (EBSD) indexing approach that can handle overlapping patterns arising from fine-scale mixtures of two crystallographically distinct but related phases. The approach relies on a combination of spherical indexing (SI) with an overlap master pattern (OMP) in which the two phases have the proper orientation relation. We illustrate the approach using a Ti-10-2-3 sample and compare results from traditional Hough-based indexing of the α and β-phases with SI maps. We show that the SI approach produces superior orientation maps, and we present a symmetry-based algorithm for the determination of the α-phase variant when experimental patterns are indexed with respect to the OMP. We illustrate the use of the OMP to determine the parent β-phase volume fraction and obtain excellent agreement with Thermo-Calc phase fraction predictions.

Key words: EBSD, indexing, Titanium, orientation relationship, parent phase determination.

1 Introduction

Electron back-scatter diffraction (EBSD) is a mature experimental technique for the determination of textures in polycrystalline materials [1]. In essence, the technique analyses the spatial arrangement and/or the intensities of Kikuchi bands on a detector and extracts the orientation of the material inside the interaction volume of the incident electron beam. Experimentally, the sample orientation in the microscope is set so as to generate a large flux of back-scattered electrons (BSEs) in the direction of the detector; practically this means that the sample is oriented at about 70° with respect to the incident beam, and the detector is positioned nearly parallel to the incident beam, at a distance of 10 to 20 mm from the sample. EBSD analysis of microstructures is most successful for those microstructures that have grain sizes several times larger than the beam interaction volume. The resulting patterns consist of Kikuchi bands superimposed on a continuous background; conventional indexing algorithms then rely on a determination of the orientation and position of the most prominent bands, as obtained from a Hough transform of the pattern [2]. Comparison against a precomputed list of inter-band angles then results in the orientation of the crystal lattice at the illumination point. An indexing approach based on Kikuchi bands depends on the ability of the algorithm to distinguish the bands above the background signal. The visibility of individual bands can be affected by local strain gradients and by surface imperfections. In addition, when the microstructure length scale is comparable to or smaller than the illumination spot size, bands from neighboring grains or other microstructure components will overlap in the same EBSD pattern which will generally confuse the indexing algorithm, since there is no mechanism to identify bands as belonging to one grain/phase or the other. Pattern overlap is commonly observed near grain boundaries, and techniques have been developed to separate the individual pattern contributions before application of High Resolution EBSD

* Marc De Graef, Department of Materials Science and Engineering, Carnegie Mellon University, 5000 Forbes Avenue, Pittsburgh, PA 15213-3890, USA.

Email addresses: wlenthe@andrew.cmu.edu (W.C. Lenthe), lionel.germain@univ-lorraine.fr (L. Germain), maria-rita.chini@irt-m2p.fr (M.R. Chini), nathalie.gey@univ-lorraine.fr (N. Gey), degraef@cmu.edu (M. De Graef).

(HR-EBSD) cross-correlation techniques to analyze local strains [3,4].

In the case of microstructures that vary on a very small length scale, which form the focus of the present paper, there is often a distinct orientation relation (OR) between the microstructure components, and this relation can become a useful aid for the indexing process, even when the beam size is significantly larger than the component size. The components may be twin variants in a finely twinned region, cementite and ferrite in fine pearlite colonies, or the typical lath structures found in α–β titanium alloys, to name just a few. The inability of standard Hough-transform based indexing algorithms (HI) to distinguish Kikuchi bands from different orientation variants or phases present in a single diffraction pattern can be circumvented by the use of the dictionary-based indexing (DI) approach [5] as well as the more recent spherical indexing (SI) algorithm [6,7]. For both of these approaches, a physics-based forward model for EBSD pattern generation [8,9] is combined with a pattern matching algorithm, based on scalar products between experimental and simulated patterns for the dictionary indexing technique [5] and spherical cross-correlations for the spherical indexing algorithm [7]. The forward model involves a Monte Carlo estimate of the directional, depth, and energy distributions of back-scattered electrons (BSEs) and a subsequent dynamical scattering simulation of the orientation distribution of the BSE yield, which we will refer to as the *master pattern*. These components are combined into an energy-weighted master pattern on the Kikuchi sphere; for each energy bin, a dynamical master pattern is computed as an integral over the depth in the sample, using the depth profile for that energy. The individual energy master patterns are then averaged with weight factors extracted from the Monte Carlo simulation. Knowledge of the detector geometry then allows for the computation of individual EBSD patterns for a given crystal lattice orientation. If the detector configuration is properly calibrated, then both pattern matching approaches, DI and SI, have the potential to index patterns with signal-to-noise ratios significantly below those for which the conventional indexing methods cease to work [10]. Furthermore, since these approaches do not look for individual Kikuchi bands in experimental EBSD patterns, but instead compare the entire pattern to simulated patterns, there is no reason why this approach should not work for fine-scale microstructures; all that is required is the substitution of the usual master

pattern by one that consists of a superposition of the component master patterns, oriented according to the proper OR. In this paper, we will demonstrate this approach for the α–β-Ti system using the Burgers OR and the spherical indexing approach.

The structure of this paper is then as follows: after introducing the experimental system and techniques in section 2, we describe, in section 3, the concept of the master pattern, and how a standard OR can be used to generate overlap master patterns; while the derivation is valid for all crystal symmetries, we focus the examples on the case of the Burgers orientation relation in bcc-hcp systems. Then we present a series of experimental EBSD observations and analyses on a Ti alloy in section 4. Finally, in section 5, we expose the advantages and drawbacks of the SI approach and discuss potential broader applications.

2 Experimental procedures

2.1 Material and Sample preparation

A sample of a Ti-10-2-3 alloy was investigated; its as-received microstructure is bimodal, containing about 13 vol. % equiaxed α nodules embedded in a two-phase matrix. The nodules are 2-5 μm in diameter and are called primary α because they were formed during the primary work in the $\alpha + \beta$ domain. The two-phase matrix results from the last solution and aging treatment. It is composed of prior β grains of about 5-10 μm partially transformed in very fine α needles called secondary α of about 0.1-0.2 μm in thickness (Fig. 1). In the prior β grains, the α and β phases are related by the Burgers orientation relation (OR).

The sample surface was prepared with care by mechanical polishing. Two final steps were used to prevent as much as possible surface hardening: A 20 min polishing step with a solution of OPS-S, followed by polishing under Ar-ions accelerated at 6 kV for 2 hours (using a PECS II from Gatan).

2.2 EBSD Pattern Acquisition

Two EBSD maps with different resolutions were measured on a Jeol 6500-F FEG SEM equipped with a Nordlys-S camera from Oxford Instruments and Aztec acquisition software. The first map was acquired on a region of interest (ROI) at the scale of the primary α nodules (ROI-1) and the second aimed to get more information at the scale of the secondary α needles (ROI-2). EBSD acquisition parameters were adapted according to the scale and are given in table 1. Background substracted EBSD patterns were saved for re-indexing with both approaches (HI and SI).

3 Theoretical Considerations

3.1 EBSD master patterns

Dynamical EBSD simulations can be rather time consuming, since, for each detector pixel, a complete N-beam dynamical scattering simulation along with a depth integration needs to be carried out [9]. One can employ either the Bloch wave approach, as in [8,9], or the scattering matrix approach (e.g., [11]) along with a suitable implementation of the Bethe perturbation theory [12] to reduce the size of the dynamical matrix. It is far more efficient, however, to pre-compute the BSE yield for all possible exit directions, and store these yields in a computationally appropriate form. In [13] and [14], two equal-area mapping techniques were introduced between a spherical surface and either a square or a regular hexagon, covering the two highest order rotational crystallographic symmetries. When the BSE yield is mapped using either of these modified Lambert projection methods, we refer to the resulting maps as EBSD master patterns. A master pattern is thus an equal-area projection from the Kikuchi sphere onto a regular polygon, which is represented numerically on a dense square or hexagonal grid of pixels; for all applications in this paper, we employ the square Lambert projection only. To facilitate the visual interpretation of a master pattern, we transform the projection to a conventional stereographic projection, but the actual computations are all

performed based on the square Lambert representation.

The master pattern is defined with respect to a standard (right-handed) Cartesian reference frame that follows the convention of the International Tables for Crystallography [15], namely that the Bravais basis vector $\mathbf{a}$ is parallel to $\mathbf{e}_x$, and the reciprocal $\mathbf{c}^*$ vector is parallel to $\mathbf{e}_z$. In the stereographic representation of the master pattern, the $\mathbf{e}_x$ axis is oriented horizontally pointing towards the right, and $\mathbf{e}_z$ is normal to the plane of the projection, pointing towards the reader. The transformation from crystallographic to cartesian quantities can be performed by means of the direct and reciprocal structure matrices, a_{ij} and b_{ij} respectively (e.g., see section 7.4.3 in [16]).

Fig. 2 shows the master patterns for α and β titanium for a sample tilt of 70° and microscope accelerating voltages of 8 and 15 kV. The patterns correspond to the highest energy bin of the master pattern, i.e., for electrons that have lost less than 1 keV of energy due to inelastic scattering processes in the material; details of the corresponding Monte Carlo and dynamical electron scattering simulations can be found in [9].

3.2 Computation of an overlap master pattern

It can be shown that the rotation matrix for the Burgers orientation relation ($\mathbf{t}^\beta = [111] \parallel [11.0] = \mathbf{t}^\alpha$ and $\mathbf{g}^\beta = (1\bar{1}0) \parallel (00.1) = \mathbf{g}^\alpha$) is given by (See appendix A for details):

$$\rho_{mk} = \begin{pmatrix} 0.642229 & 0.642229 & -0.418432 \\ 0.295876 & 0.295876 & 0.908248 \\ 0.707107 & -0.707107 & 0. \end{pmatrix}; \tag{1}$$

the corresponding unit quaternion is given by

$$q_\rho = [0.696079, -0.580162, -0.404242, -0.124394], \tag{2}$$

with the scalar part as the first entry.

The OR rotation matrix ρ_{mk} allows us to obtain an expression for the transformation of the α master pattern into the reference frame of the β structure. As explained in appendix B, the master pattern is represented on a square Lambert array of $(2N+1)^2$ pixels; the edge length of the square master pattern is $\sqrt{2\pi}$ [13]. Therefore, the cartesian coordinates (a, b) corresponding to pixel (i, j) (with $-N \leq i, j \leq N$, $i, j \in \mathbb{Z}$, and the origin at the center of the projection) are given by:

$$(a, b) = \frac{1}{N}\sqrt{\frac{\pi}{2}}(i, j).$$

If we wish to determine the contribution of the α structure to a given pixel (i, j) of the β master pattern, then we need to first determine the direction on the hemisphere corresponding to this point, which is accomplished using the inverse mapping $\mathcal{L}^{-1}$ of equations B.7 in appendix B. The direction cosines c_k are thus given by $c_k = (x, y, z) = \mathcal{L}^{-1}[a, b]$. The orientation relation is then applied by transforming the direction cosines according to the matrix ρ_{mk} to obtain $c'_m = \rho_{mk} c_k$. The final step then involves transformation of c'_m to the master pattern of structure B, which is performed as $(a', b') = \mathcal{L}[c'_m]$. Since the point (a', b') will not, in general, coincide with a grid point of the α master pattern, we extract the BSE yield from the α pattern by means of bilinear interpolation, which, in the limit of a fine pixel spacing, is permitted since the modified Lambert projections are equal area projections of the direction hemisphere.

If we represent the master pattern by the symbol $\mathcal{M}$ and use a superscript to indicate the phase α or β, then we can write the intensity at pixel location (i, j) of the overlap master pattern $\mathcal{M}^O$ as:

$$\mathcal{M}^O(i, j) = f_\beta \mathcal{M}^\beta(i, j) + (1 - f_\beta)\mathcal{M}^\alpha \left(N\sqrt{\frac{2}{\pi}}\, \mathcal{L}\left[\boldsymbol{\rho}\, \mathcal{L}^{-1}\left[\frac{1}{N}\sqrt{\frac{\pi}{2}}(i, j) \right] \right] \right), \tag{3}$$

where f_β is the desired volume fraction of phase β, and $\boldsymbol{\rho}$ is the OR matrix ρ_{mk}. It is clear from this relation that phase β is kept in its standard orientation with respect to the Cartesian reference frame, and the master pattern of phase α is rotated according to the orientation relation. This relation is implemented in the *EMEBSDoverlap* program available as part of the open source *EMsoft* simulation package (`http://vbff.materials.cmu.edu/EMsoft`).

The result of applying this formalism to the master patterns for the α and β titanium phases

is shown in Fig. 3. In (a) and (b), the α and β master patterns are shown as stereographic projections; the α pattern has been rotated by the Burgers OR matrix $\boldsymbol{\rho}$, bringing the (00.1) plane normal parallel to the cubic $(1\bar{1}0)$ plane normal and the [11.0] direction along the cubic [111] direction. In (c), the rotational symmetry elements of both phases are represented on a stereographic projection; it is clear that the only surviving rotational symmetry element in the overlap pattern is the cubic two-fold axis along $[1\bar{1}0]_\beta$, represented by a dashed line. The symmetry of the overlap master pattern is thus monoclinic, with point group $\mathbf{2/m}$; however, for our purposes we will only need the pure rotational sub-group $\mathbf{2}$.

There are twelve possible orientations of the α-Ti phase with respect to the β-Ti phase; the Burgers ORs and standard variant labels are listed in Table 2, along with the rotation unit quaternions that rotate variant $V1$ into the orientation of variant Vj; these rotations will become important in the analysis of indexed orientation data in section 4.3. Note that there are two rotations that are part of the cubic rotational symmetry group $\mathbf{432}$ for each variant; they are related to each other by a 180° rotation around the $[1\bar{1}0]_\beta$ axis. Fig. 4 shows all twelve overlap master patterns with the α-phase in each of the Burgers ORs; all projections are oriented in the standard orientation for the β-phase. Since the overlap pattern has rotational symmetry group $\mathbf{2}$ of order 2, and the parent β-phase $\mathbf{432}$ of order 24, one could be able to index intricate $\alpha - \beta$ structures using the monoclinic overlap pattern to determine the main individual α orientation as well as the underlying β-phase parent orientation.

To understand how the overlap pattern orientation in the triclinic fundamental zone (FZ) (eventually reduced to the monoclinic FZ) can be used to retrieve both the orientation of the α and β-phases, let us display the FZ for the α and β-phases in a 3D stereographic projection (Fig. 5(a)). The red frame outlines the cubic FZ, the green frame the hexagonal FZ rotated into the Burgers orientation for variant $V1$. The colored spheres represent the rotations that bring variant $V1$ into coincidence with variant Vj, i.e., corresponding to the quaternions in Table 2; the larger spheres all fall inside a monoclinic FZ (a lens-shaped region outlined in blue) that is oriented such that its two-fold rotation axis falls along the $[1\bar{1}0]_\beta \parallel [00.1]_\alpha$ direction which is depicted in dark blue. The color code at the top of Fig. 5 is used next to generate orientation variant maps based on indexing with the overlap master

pattern. It is clear from both Table 2 and Fig. 5 that the variant rotations q_{Vj} are those cubic symmetry operators that fall inside the rotated monoclinic fundamental zone. The equivalent rotations that fall outside of the monoclinic FZ are represented by smaller spheres of the same color. A more detailed analysis in terms of co-set decompositions is presented in Appendix C. Fig. 5(b) shows all 24 equivalent cubic fundamental zones along with the cubic symmetry elements using the first color legend in Table 2; 15 of the zones fall completely inside the stereographic projection sphere, the other 9 straddle the surface of the sphere and re-enter on the opposite side. For each α-variant, there are two cubic FZs with the same color in Fig. 5(b); they are related to each other by the two-fold monoclinic rotation $2_{[1\bar{1}0]}$. An animated mp4 version of both stereographic projections is available as Supplementary Material (DOI 10.1184/R1/8976410).

The orientation of each individual α-variant j with respect to the standard reference frame is given by the product $q_{Vj}q_\rho$, where q_ρ is defined in eq. 2. When the β grain is rotated into orientation q_β, the α-variants are rotated into orientations $q_{Vj}q_\rho q_\beta$. For the β-phase, the corresponding orientation, $q_{Vj}q_\beta$, does lie in the cubic fundamental zone only for $j = 1$. This then suggests the following algorithm for the determination of both the parent β orientation and the α variant number: when an EBSD measurement produces an orientation q_m when indexed without rotational symmetry, this point will fall inside one of the 24 disjoint regions of orientation space. Those regions are labeled/colored by the α-phase variant IDs, which is essentially what is illustrated in Fig. 5(b), where each sphere lies at the center of its own cubic fundamental zone. When the quaternion q_m is reduced to the cubic fundamental zone, we obtain q_β, i.e., the parent phase orientation. We also have that q_m must be equal to $q_{Vj}q_\beta$ for some value of j; thus, when we compute $q_m q_\beta^*$, we obtain q_{Vj} which labels the α orientation variant as variant j. The identification of the variant number is then simply a matter of determining which fundamental zone q_{Vj} belongs to. Due to the monoclinic overlap master pattern symmetry, there are two equivalent zones in orientation space for each α-variant.

Hough-based re-indexing (HI) of the patterns was performed with Aztec 3.2 on a Windows workstation using 5 CPU threads (Intel Xeon CPU E5-2630 v4 @ 2.20GHz). A Hough resolution of 60 and the "refined accuracy" mode [17] were used. Ten bands were detected and a solution was accepted only if a minimum of 6 bands matched a theoretical pattern. To evaluate the ability of Aztec to index overlap patterns, indexing was performed separately with respect to the α and β-phases.

In addition to the standard HI approach, Spherical Indexing (SI) was used to obtain the orientations of the α and β-phases in both ROIs. Spherical indexing uses the spherical harmonic transform of the Kikuchi master pattern [6,7] as well as the experimental pattern to determine the 3D rotation that brings the latter into coincidence with the former. A single EBSD pattern from an α-nodule was extracted from each ROI and used to refine the detector parameters (pattern center and scintillator-sample distance); the relevant parameters used for spherical indexing are listed in Table 1. All spherical indexing was carried out on a Linux workstation using 24 CPU threads (Intel Xeon CPU E5-2670 v3 @ 2.30GHz) and the timing includes an orientation refinement step, as described in [7].

4 Experimental results and data analysis

In this section, we compare conventional Hough-based Indexing (HI) with spherical indexing (SI) on two experimental EBSD data sets for a Ti 10-2-3 alloy. First we analyze the results of indexing with respect to the master patterns of the individual α and β-phases. Then, we show how the overlap master pattern approach can be used to estimate the volume fraction of the β-phase in the transformed β grain components of the microstructure. Finally, we re-analyze the data using the overlap master pattern approach to identify both the parent β orientation and the α orientation variants.

As a first step, we indexed the experimental patterns for the two ROIs with respect to the α and β-phases, using the standard point group symmetries of **622** and **432**, respectively, to reduce the orientations to the corresponding fundamental zones. EBSD maps colored according to the key given in the Inverse Pole Figure (IPF) map relative to the sample normal are shown in Fig. 6 for ROI-1 and Fig. 7 for ROI-2. The top row shows the results of Hough-based indexing using the Aztec 3.2 software from Oxford; the second row shows the spherical indexing results. It is clear that the results of spherical indexing show significant improvement over those of Hough-based indexing. The HI α map shows a reasonable indexing rate in the nodules but a very low rate in the fine α needles; this is probably the result of superimposed and low quality patterns in this region. The SI results in a very high indexing rate showing large domains with a single orientation. In those intricate needle structures one should expect to find more orientations locally. This means that SI has indexed the crystal having the largest volume fraction in the diffraction volume. The most striking result is obtained when indexing of the β-phase is considered: with the HI approach, 84% of the sampling points were un-indexed, compared to only 3% for the SI approach.

EBSD also offers an insight on the microstructure. To this purpose, different indicators can be derived from the indexing results. In (e) and (f) an indicator derived from SI is presented. The cross-correlation index (CCI) [7,18] maps are shown on a common intensity scale; the intensity represents the spherical harmonic cross-correlation value for the best matching orientation in each pixel [7]. The band contrast (BC) map is shown in (g); it is obtained from Aztec and corresponds to the ratio between the detected band intensity over the average intensity of the background substracted pattern. The pattern quality map is shown in (h) and corresponds to the pattern sharpness parameter (IQ) as defined in [19]. Most indicators are in general agreement and show the highest values for the nodular α regions, which produced the clearest EBSD patterns. The most informative microstructure image is provided by the CCI map when indexing is performed against the α patterns; this is particularly obvious when looking at Fig. 7(e).

Fig. 8(a) shows a background-subtracted EBSD pattern from the location marked by a white square in Fig. 9(b); averaging over 11×11 patterns centered on the pattern in (a) results in the pattern in Fig. 8(b). Using the refined β orientation for this colony from the analysis described in the next section, resulting in (Bunge) Euler angles $(197.91°, 124.05°, 51.23°)$, the EBSD patterns in (c) and (d) were computed for 100% β-phase (c), and 50% (d), using eq. 3 to compute the overlap master pattern. Note the reasonable agreement between the pairs of nearly parallel arrowed bands in (b) and (d); in (c), the second Kikuchi band is completely absent, indicating that this band is associated with the α-phase. Varying the volume fraction, f_β, of the β-phase master pattern in equation 3 and computing the normalized dot product (i.e., the dot product between 1-D pattern intensity vectors of unit Euclidean length) between the averaged pattern in (b) and the simulated patterns results in the plot in Fig. 8(e). The simulated pattern corresponding to the maximum dot product value, i.e., the highest similarity between simulated and experimental patterns is shown in (f). It is obtained for a β volume fraction of 35% inside the diffracting volume in the β grains, which corresponds to a fraction of 30% in the whole microstructure (accounting for the 13% fraction of primary α). This fraction was compared with the β fraction at thermodynamic equilibrium at 500°C predicted by Thermo-Calc [20]. Indeed, as the aging was performed at 500°C for $8h$ we can assume that the microstructure is close to thermodynamical equilibrium before quenching. This means that the volume fraction at the highest dot product value provides a reasonable estimate of the real fraction in the transformed β grains. The theoretical phase fraction calculation was aimed just at providing a reasonable estimate for comparison with the fraction determined by pattern overlap SI; the close agreement between the two values is perhaps fortuitous, but nevertheless encouraging. Furthermore, using the $f_\beta = 35\%$ overlap master pattern results in an overall increased CCI value by about one percent, indicating a better pattern match. In the following section, we will use the overlap master pattern with $f_\beta = 0.35$ to perform the final indexing step.

Fig. 9 shows the results of spherical indexing with respect to the overlap master pattern (SI-OMP) $\mathcal{M}_O$ for a β volume fraction of $f_\beta = 35\%$ and a bandwidth of 263, the largest value used in this study. The top row shows $[001]_\beta$ IPF maps for both regions of interest after reduction of the orientations to the cubic fundamental zone; this map clearly shows that the β-phase sub-grains have a $[111]_\beta$ direction close to normal to the sample surface. Fig. 9(c) and (d) show the α variant maps color-coded by variant number (see Table 2 for RGB color definitions). For each experimental pattern the algorithm described in section 3 was applied; the resulting orientation was then reduced to the rotated monoclinic fundamental zone and compared to the variant orientations shown in Fig. 5. The color legend emphasizes a grouping of variants that have a common $\langle 111 \rangle_\beta$ direction. The bottom row in Fig. 9 shows the variant map using the second color legend, namely in terms of pairs of variants that have a common $\{110\}_\beta$ plane. One can see that the $\langle 111 \rangle_\beta$ grouping forms larger clusters which is typical of this kind of structures [21].

As a consistency check, the orientations q_m obtained from SI-OMP can be converted to the standard reference frame for the α-phase by means of the following transformation: $q_\alpha = q_{Vi} q_\rho q_\beta$ where q_{Vi} is the appropriate quaternion from Table 2. Applying this transformation to each of the orientations q_m, using the correct variant ID for each pattern, results in an α-phase IPF map, after reduction of the q_α orientations to the hexagonal fundamental zone, that is identical to the one obtained by direct indexing with respect to the α-phase master pattern (Fig. 6(e)).

Finally, Fig. 10 shows a color map of both regions of interest; the color is determined by the highest value of the cross-correlation. In red regions, the spherical indexing with respect to the hexagonal α-phase produced the highest cross-correlation values; green regions correspond to the β-phase. The blue regions have the highest cross-correlation for the overlap master pattern, i.e., they correspond to regions where both phases are present. One can see that the nodules are correctly identified and that some retained β phase is found near the nodules. This is because, when the nodules formed, β stabilizer was rejected in their vicinity, favouring

a higher fraction of retained β.

5 Discussion

5.1 Computation time

Execution times (expressed as patterns indexed per second) are listed in Table 3 for both regions of interest and for the three master patterns and for Hough re-indexing. In general, SI is more computationally intensive than HI. The direct comparison reveals that SI takes approximately twice the time required by HI. However, the Aztec software uses only 5 cores among the 20 available and therefore the HI execution time could be reduced even further.

HI indexing is relatively independent of symmetry but depends instead on the number of phases simultaneously considered for indexing. For the SI approach, the execution time depends on the band width, i.e., the maximum ℓ value selected for the spherical harmonic expansion. Since the SI cross-correlation takes into account the symmetry of the master pattern, the hexagonal α-phase indexing is slightly faster than the others; this is due to the fact that the highest rotational order equals 6 for the hexagonal system and 4 for the cubic one. In the absence of symmetry, the overlap master pattern indexing rate is slower than for the α and β-phases. Note that triclinic symmetry was used for the indexing based on the overlap master pattern; some execution speed could be gained by indexing with respect to the monoclinic rotational group **2**.

5.2 Deviations from the Burgers OR

The SI-OMP method assumes that the Burgers OR is strictly respected between the α and β phases. This assumption was verified a posteriori by comparing the orientation of all pixels in the SI-α map with those at the same position in the SI-β map. The result is presented in the map and histogram in Fig. 11. The deviation angle from the Burgers OR is represented

with the color scale below the histogram. This map reveals that the Burgers OR is very often respected below 2° with a peak at 0.85°. The tail of the distribution reaches 6°, but is only observed for the α precipitates that have nucleated at the transformed β boundaries (the so-called α_{GB}). Thus, it appears that a deviation of about 2° from the Burgers OR does not decrease significantly the SI-OMP ability to index both phases correctly. Therefore, this method can certainly be extended to systems with a high twin density for which the OR is more strictly satisfied. The case of steel (e.g., pearlite) promises to be more challenging, since a deviation to the OR may be as high as $3 - 5°$ [22].

5.3 Sensitivity to pseudo-symmetry

The concept of indexing with respect to an overlap master pattern is new, and one must ask the question: what kind of indexing errors should we expect to encounter? Every indexing approach, including the Hough-based algorithm, may incorrectly index patterns when certain conditions complicate unambiguous indexing of particular orientations. Such pseudo-symmetry (PS) issues have been labeled "systematically mis-indexed pixels," to distinguish them from randomly mis-indexed pixels [23]. If the potential PS cases can be identified, then one can propose a post-processing solution to resolve them.

Within the context of spherical indexing, it was shown in [18] that potential PS issues can be predicted by means of the auto-correlation of the master pattern; i.e., if the same master pattern is used for both sets of spherical harmonic coefficients in the cross-correlation, then the resulting auto-correlation produces an array of intensities in Euler space that has primary maxima at the locations of all the rotational symmetry elements of the crystal structure, and secondary maxima for misorientations that may reveal themselves in the form of PS issues during indexing.

The result of the auto-correlation analysis of the overlap master pattern are summarized in Table 4; the table lists the auto-correlation values that are larger than 0.5 (in the range $[-1, 1]$) and the quaternions corresponding to the misorientations for which they occur. The

top two quaternions have an auto-correlation of 1.0, indicating that they correspond to the rotational symmetry elements of the (monoclinic) overlap master pattern; they are the identity operation and the two-fold rotation $2_{[1\bar{1}0]}$. The other entries in the table are ranked with respect to descending auto-correlation value; the final column in the table interprets the quaternions as axis angle pairs.

The next highest auto-correlation value is related to the 60°@[111] rotation, which is also the most frequently encountered PS for cubic crystals. The three other misorientations are characteristic of the SI-OMP operation and occur for pure α patterns (or at very low β fractions). Then, SI-OMP indexes the α-phase correctly, but chooses the cubic parent randomly. As a result, the cubic phase indexing presents one of the misorientations typical of β grains having an α variant in common, as described in [24].

The misorientation angle distribution provides a means to estimate the occurrence of PS, as shown for the ROI-1 data set in Fig. 12. The observed peaks are at the same angles as those listed in Table 4, namely 10.5°, 49.5° and 60°. At a first glance, one may think that the method produces a lot of mis-indexations. However, a careful look shows that these are mainly located in the α nodules. When the latter are removed from the data set, the histogram peaks are reduced drastically. The small amount of mis-indexed points that remains can be cleaned using the same methods used to clean conventional HI EBSD data sets.

5.4 Indexing of more complex microstructures

When the microstructure length scale becomes very fine, it is possible to have more than one α-phase variant inside the beam interaction volume. In terms of an overlap master pattern, this would mean that three or more patterns need to be combined. For microstructures in which the α-variants have a common $\{110\}_\beta$ plane, the overlap master patterns for variants V1 and V10 can be combined into a "double overlap" master pattern with a resulting orthorhombic **222** rotational symmetry. The same indexing approach described in this paper

could then be used, and there will be six points inside the orthorhombic fundamental zone that correspond to the six potential variant pairs. If the α-variants are organized with a common $[111]_\beta$ direction, then there are potentially three variants simultaneously inside the interaction volume, and a "triple overlap" master pattern could be constructed that contains variants V1, V2 and V3. The rotational symmetry of this overlap pattern is the trigonal point group **32** of order 6, corresponding to the four groupings of variants in Table 2. When indexed using the triple overlap master pattern, there would be four potential locations inside the trigonal fundamental zone that correspond to the four different groupings. Indexing of ROI-1 and ROI-2 using these double and triple overlap master patterns is currently being explored.

The proposed approach based on the overlap master pattern will likely work when the volume fraction of the parent phase present in the microstructure is sufficiently high so that its Kikuchi bands become noticeable in the overlap EBSD patterns. In such cases, a weighted average of the master patterns is likely to produce a good prediction of the actual EBSD patterns when both phases are present in the beam interaction volume. This will also be the case for finely twinned systems, where both twin variants have similar volume fractions. For fcc twins, for instance, the overlap master pattern has trigonal **32** rotational symmetry, and we anticipate that the SI-OMP technique proposed in this paper will work well for nano-twinned materials.

6 Conclusions

As is obvious from the timing information shown in Table 3, the spherical indexing approach is generally slower than Hough-based reindexing, in particular if a large band width (i.e., spherical harmonic truncation) is used. However, this increased computation time compared to the HI approach is more than offset by the quality of the indexing results. SI is robust against noise and, more importantly, the approach can be used with overlap master patterns, which sets it apart from the more traditional indexing.

The new indexing approach proposed in this paper is based on a combination of the overlap master pattern concept and indexing based on full pattern comparisons, which includes dictionary and spherical indexing approaches. Standard Hough-based indexing approaches are not able to handle EBSD patterns from overlapping phases, although one could conceivably extend the HI technique to handle overlap patterns for cases in which a fixed orientation relation is expected. Our current implementation using the overlap master pattern and spherical indexing does not require significantly more computation time than standard SI indexing, nor does it require modifications to the indexing algorithm; thus, full pattern indexing is likely to be the more efficient approach for fine-scale microstructures. Furthermore, Spherical indexing provides a substantially higher confidence level for both the α and β-phases than Hough indexing.

Spherical Indexing showed a very good ability to index patterns, especially in the very fine needle structures where the Hough Indexing rate was very low. The orientation indexing corresponds to the crystal having the highest volume fraction in the diffracting volume.

The agreement between the β-phase fraction derived from the spherical indexing approach and the value predicted from Thermo-Calc calculations suggests that the overlap master pattern may provide a convenient approach to phase fraction estimation.

The auto-correlation of the overlap master pattern generates a list of potential pseudo-symmetry misorientations that may show up as systematically mis-indexed pixels in orientation maps; knowledge of the potential misorientations also suggests the steps that need to be taken to correct such pixels. Similarly, the computation of the cross-correlation between master patterns from two different phases, e.g., α and β-Ti, can identify orientations for which an indexing algorithm may not be able to distinguish easily between the two phases. As such, it provides more information than the standard HI approach, since two accurate orientations can be obtained from a single pattern.

The source code for the spherical indexing algorithm will be made available as a standalone package and as part of the 4.3 release of the EMsoft source code package, available from the following URL: http://vbff.materials.cmu.edu/EMsoft. All experimental data files for ROI-1

and ROI-2 as well as the master patterns for α and β-phases, the overlap master patterns for 35 and 50 vol% β-phase, all input files used for spherical indexing and the indexing results files (in .ctf and .ang formats) are made available via CMU's KiltHub data repository at DOI 10.1184/R1/8976410.

Acknowledgements

WCL and MDG gratefully acknowledge funding from a DoD Vannevar-Bush Faculty Fellowship (# N00014-16-1-2821) as well as the computational facilities of the Materials Characterization Facility at CMU under grant # MCF-677785. MDG would also like to acknowledge financial support for a visit to the Université de Lorraine through the program "Investment for the future" operated by the National Research Agency (ANR) and referenced by ANR-11-LABX-0008-01 (LabEx DAMAS). Dr J. Zollinger is acknowledged for the ThermoCalc calculation.

References

[1] A.J. Schwartz, M. Kumar, B.L. Adams, and D.P. Field, editors. *Electron Backscatter Diffraction in Materials Science*. Springer, 2009.

[2] N.C. Krieger Lassen. Image processing procedures for analysis of electron backscattering patterns. *Scanning microscopy*, 6:115–121, 1992.

[3] Vivian Tong, Jun Jiang, Angus J. Wilkinson, and T. Ben Britton. The effect of pattern overlap on the accuracy of high resolution electron backscatter diffraction measurements. *Ultramicroscopy*, 155:62 – 73, 2015.

[4] Josh Kacher, Brent Adams, David Fullwood, and Colin Landon. *Separating Coincident Electron Backscatter Diffraction Patterns Near Interfaces*, volume 201, pages 147 – 154. American Ceramic Society, 11 2008.

[5] Y.H. Chen, Park S.U., D. Wei, G. Newstadt, M. Jackson, J.P. Simmons, M. De Graef, and A.O. Hero. A dictionary approach to EBSD indexing. *Microsc. MicroAnal.*, 21:739–752, 2015.

[6] Ralf Hielscher, Felix Bartel, and Thomas Benjamin Britton. Gazing at crystal balls - Electron backscatter diffraction indexing and cross correlation on a sphere. *arXiv e-prints*, page arXiv:1810.03211, 2018.

[7] W.C. Lenthe, S. Singh, and M. De Graef. A spherical harmonic transform approach to the indexing of electron back-scattered diffraction patterns. *Ultramicroscopy*, 2019 (under review).

[8] A. Winkelmann, C. Trager-Cowan, F. Sweeney, A.P. Day, and P. Parbrook. Many-beam dynamical simulation of electron backscatter diffraction patterns. *Ultramicroscopy*, 107:414–421, 2007.

[9] P.G. Callahan and M. De Graef. Dynamical EBSD patterns Part I: Pattern simulations. *Microscopy and MicroAnalysis*, 19:1255–1265, 2013.

[10] S.I. Wright, M.M. Nowell, S.P. Lindeman, P.P. Camus, M. De Graef, and M.A. Jackson. Introduction and comparison of new EBSD post-processing methodologies. *Ultramicroscopy*, 159:81–94, 2015.

[11] Y.N. Picard, M. Liu, J. Lammatao, R. Kamaladasa, and M. De Graef. Theory of dynamical electron channeling contrast images of near-surface crystal defects. *Ultramicroscopy*, 146:71–78, 2014.

[12] A. Wang and M. De Graef. Using Bethe potentials in the scattering matrix for defect image simulations. *Microscopy and MicroAnalysis*, 20 (suppl 3):1030–1031, 2014.

[13] D. Roşca. New uniform grids on the sphere. *Astronomy & Astrophysics*, 520:A63, 2010.

[14] D. Roşca and M. De Graef. Area-preserving projections from hexagonal and triangular domains to the sphere and applications to electron back-scatter diffraction pattern simulations. *Modeling and Simulations in Materials Science and Engineering*, 21:055021, 2013.

[15] T. Hahn, editor. *The International Tables for Crystallography Vol A: Space-Group Symmetry.*, volume A. Kluwer Academic Publishers, Dordrecht, 1989.

[16] M. De Graef and M.E. McHenry. *Structure of Materials: An Introduction to Crystallography, Diffraction, and Symmetry.* Cambridge University Press, 2nd edition edition, 2012.

[17] K Thomsen, N.H. Schmidt, Angus Bewick, Klaus Larsen, and J Goulden. Improving the accuracy of orientation measurements using EBSD. *Microscopy and Microanalysis*, 19:724–725, 2013.

[18] W.C. Lenthe, S. Singh, and M. De Graef. Prediction of potential pseudo-symmetry issues in the indexing of electron back-scatter diffraction patterns. *J. Appl. Cryst.*, 2019 (under review).

[19] N.C. Krieger Lassen, D. Juul Jensen, and K. Conradsen. On the statistical analysis of orientation data. *Acta Cryst. A*, 50:741748, 1994.

[20] Thermo-calc software ttti3, thermotech ti-based alloys database version 3.

[21] S. C. Wang, M. Aindow, and M. J. Starink. Effect of self-accommodation on / boundary populations in pure titanium. *Acta Materialia*, 51:2485–2503, 2003.

[22] G. Nolze. Irrational orientation relationship derived from rational orientation relationships using EBSD data. *Crystal Research and Technology*, 43(1):61–73, 2008.

[23] L.N. Brewer and J.R. Michael. Risks of "cleaning" electron backscatter diffraction data. *Microscopy Today*, 18:10–15, 2010.

[24] Tao Liu, Lionel Germain, Julien Teixeira, Elisabeth Aeby-Gautier, and Nathalie Gey. Hierarchical criteria to promote fast and selective GB precipitation at grain boundaries in -metastable Ti-alloys. *Acta Materialia*, 141(Supplement C):97–108, 2017.

[25] J.W. Christian and S. Mahajan. Deformation twinning. *Progress in Materials Science*, 39:1 – 157, 1995.

[26] Shoayb Ziaei, Qifeng Wu, and M Zikry. Orientation relationships between coherent interfaces in hcp–fcc systems subjected to high strain-rate deformation and fracture modes. *Journal of Materials Research*, 30:2348–2359, 2015.

[27] G.J. Shiflet and J.H. van der Merwe. The role of structural ledges at phase boundaries—ii. f.c.c.-b.c.c. interfaces in nishiyama-wasserman orientation. *Acta Metallurgica et Materialia*, 42:1189 – 1198, 1994.

[28] W.G. Burgers. On the process of transition of the cubic-body-centered modification into the hexagonal-close-packed modification of zirconium. *Physica*, 1:561–586, 1934.

Tables

	ROI-1	ROI-2
Microscope Voltage	15 kV	8 kV
Sample tilt	70.0°	70.0°
Detector Tilt	0°	0°
Pattern Size	336×256	336×256
Pattern Center	(0.50247, 0.77138, 0.51559)	(0.50192, 0.70332, 0.51217)
Scan size	227×170	177×181
Scan Step Size	0.15 μm	0.05 μm
Exposure time	24.4 ms	122.0 ms
Nb of averaged frames	1	2

Table 1

Experimental acquisition parameters (Oxford Aztec) for both regions of interest (ROI-1/ROI-2).

j	$\mathbf{g}_\beta \parallel (00.1)_\alpha$	$\mathbf{t}_\beta \parallel [11.0]_\alpha$	$\pm q_{1\to j}$	$\langle 111\rangle_\beta$ grouping	$\{110\}_\beta$ grouping
1	$(1\bar{1}0)_\beta$	$[111]_\beta$	$[1,0,0,0]$, $[0,s,\bar{s},0]$	255, 0, 0	255, 0, 0
2	$(10\bar{1})_\beta$	$[111]_\beta$	$[h,\bar{h},\bar{h},\bar{h}]$, $[0,0,s,\bar{s}]$	255, 80, 80	0, 225, 0
3	$(01\bar{1})_\beta$	$[111]_\beta$	$[h,h,h,h]$, $[0,\bar{s},0,s]$	255, 160, 160	225, 225, 0
4	$(110)_\beta$	$[\bar{1}11]_\beta$	$[0,1,0,0]$, $[s,0,0,s]$	0, 225, 0	0, 0, 255
5	$(101)_\beta$	$[\bar{1}11]_\beta$	$[h,h,h,\bar{h}]$, $[0,0,s,s]$	80, 255, 80	255, 130, 48
6	$(01\bar{1})_\beta$	$[\bar{1}11]_\beta$	$[h,\bar{h},h,\bar{h}]$, $[s,0,\bar{s},0]$	160, 255, 160	255, 255, 160
7	$(110)_\beta$	$[1\bar{1}1]_\beta$	$[0,0,1,0]$, $[s,0,0,\bar{s}]$	225, 225, 0	160, 160, 255
8	$(10\bar{1})_\beta$	$[1\bar{1}1]_\beta$	$[h,\bar{h},h,h]$, $[s,s,0,0]$	245, 245, 80	160, 255, 160
9	$(011)_\beta$	$[1\bar{1}1]_\beta$	$[h,\bar{h},\bar{h},h]$, $[0,s,0,s]$	255, 255, 160	70, 255, 255
10	$(1\bar{1}0)_\beta$	$[11\bar{1}]_\beta$	$[0,0,0,1]$, $[0,s,s,0]$	0, 0, 255	255, 160, 160
11	$(101)_\beta$	$[11\bar{1}]_\beta$	$[h,h,\bar{h},h]$, $[s,\bar{s},0,0]$	80, 80, 255	255, 190, 90
12	$(011)_\beta$	$[11\bar{1}]_\beta$	$[h,h,\bar{h},\bar{h}]$, $[s,0,s,0]$	160, 160, 255	190, 255, 255

Table 2

Orientation relations for the 12 variants of the Burgers OR, along with the rotation unit quaternions $\pm q_{1\to j}$ (using $h = 1/2$ and $s = 1/\sqrt{2}$) that bring variant 1 into coincidence with variant j. The final columns show the RGB color values used for each variant in this paper for two different variant groupings, by common $\langle 111\rangle_\beta$ direction (four groups) or common $(110)_\beta$ plane (six groups).

MP	RPG	SI bw=88		SI bw=158		SI bw=263		Hough re-indexing
		ROI-1	ROI-2	ROI-1	ROI-2	ROI-1	ROI-2	
α	**622**	270.6	227.8	44.1	43.8	7.9	7.9	457.3
β	**432**	248.5	203.2	38.7	38.7	5.4	6.7	489.9
$\alpha + \beta$	**1**	51.3	51.8	16.1	16.2	2.4	2.3	—

Table 3

Comparison of the indexing times for the Hough (re-indexing) and spherical indexing approaches in units of patterns per second (38,590 patterns in ROI-1, 32,037 in ROI-2). HI computations carried out on a 20-core Linux platform (Intel Xeon CPU E5-2670 v3 @ 2.20GHz); SI computations carried out on a 24-core Linux platform (Intel Xeon CPU E5-2670 v3 @ 2.30GHz). [MP = master pattern, RPG = rotational point group]

auto	q	Interpretation
1.0000	$[1.000000, 0.000000, 0.000000, 0.000000]$ $[0.000000, -0.707027, 0.707187, 0.000000]$	Monoclinic Symmetry operators
0.7940	$[0.000000, 0.577846, 0.577646, 0.576558]$ $[0.000000, -0.407715, -0.407662, 0.817056]$	$60°$@$[111]$
0.7594	$[0.000000, 0.704240, 0.704026, 0.091610]$	$10.51°$@$[1\bar{1}0]$, α pattern corresponding but incorrect β pattern
0.7485	$[0.000000, 0.296590, 0.296437, 0.907832]$ $[0.000000, -0.642011, -0.641857, 0.419333]$	$49.59°$@$[1\bar{1}0]$, α pattern corresponding but incorrect β pattern
0.7335	$[0.866055, \pm 0.353466, \mp 0.353570, \mp 0.000028]$ $[0.499949, \pm 0.612303, \mp 0.612483, \mp 0.000045]$	$60°$@$[1\bar{1}0]$

Table 4

Auto-correlation values and misorientations (in the quaternion representation) for the highest values (above 0.5). The final column expresses the quaternions as axis-angle pairs that have important meanings in the α–β system. Note that the quaternions do not correspond to exact representations due to the finite step size in the Euler space used for the auto-correlation computation (band width 158).

Figures

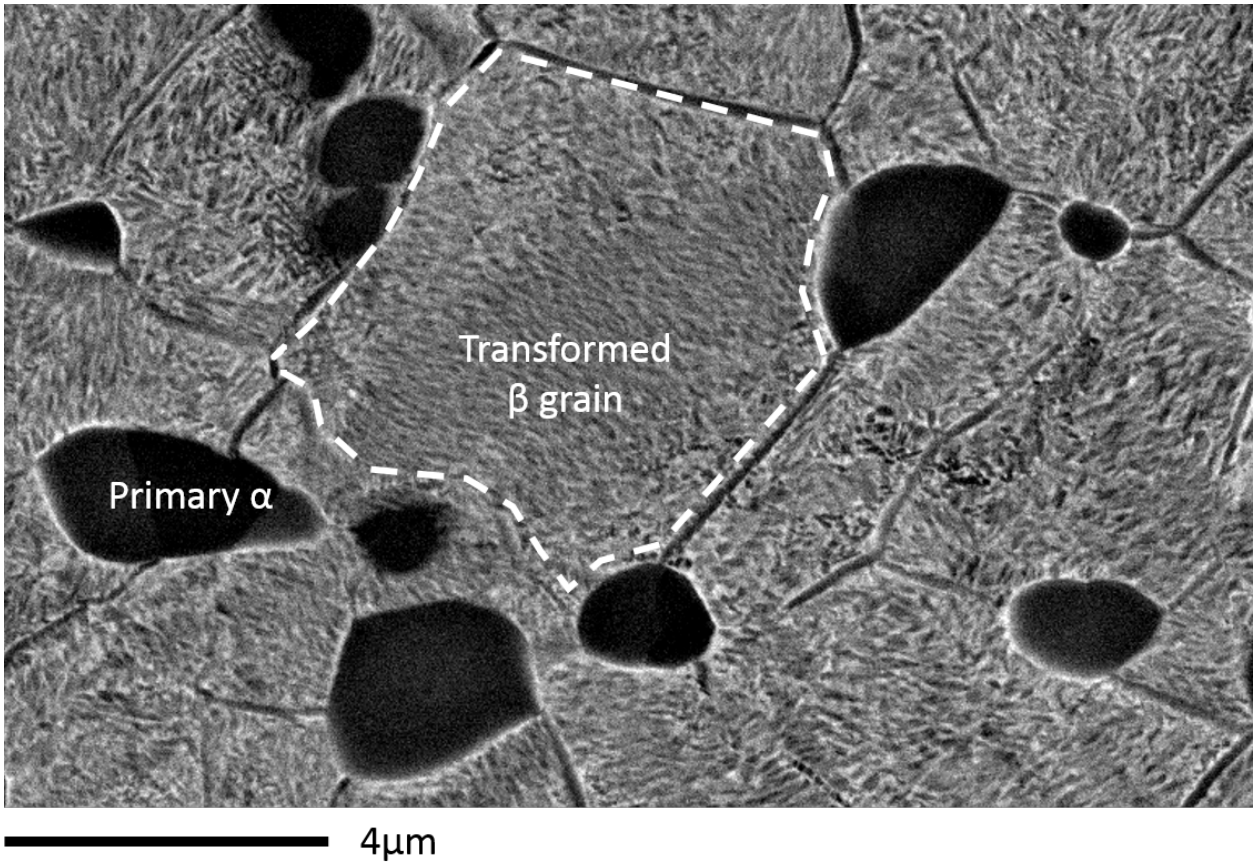

Fig. 1. Microstructure of the Ti-10-2-3 alloy; equiaxed primary α nodules are dark in this BSE image. Transformed β grains contain secondary α needles either organized in a colony or in a basket-weave structure (the residual β phase is white).

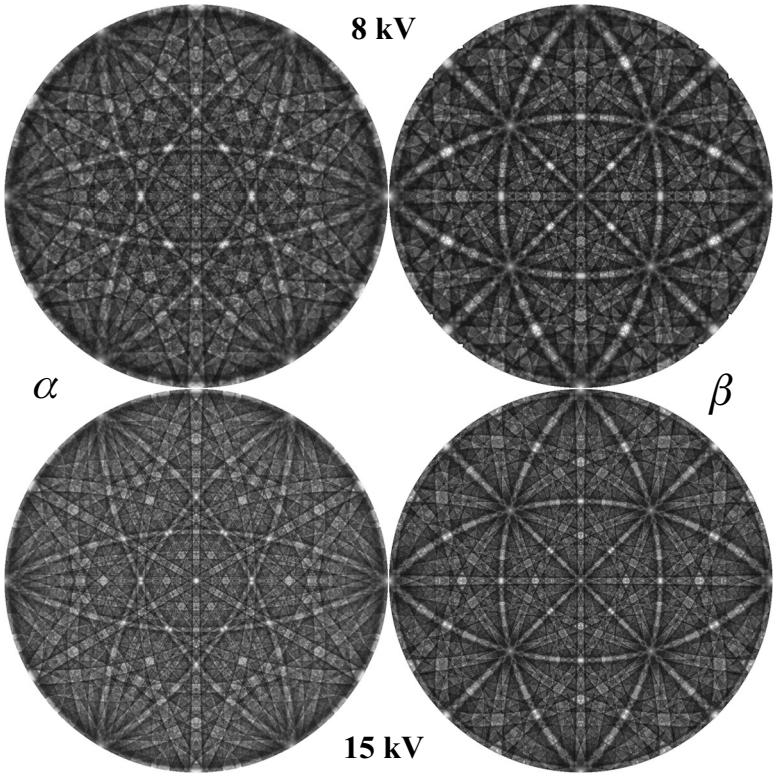

Fig. 2. EBSD master patterns for 8 kV (top row) and 15 kV (bottom row) microscope accelerating voltage for the α-Ti phase (left column) and β-Ti (right column). The crystallographic **a** axis points towards the right and $\mathbf{c}^*$ is normal to the projection plane. The patterns show the back-scattered electron distributions for electrons that have lost less than 1 keV.

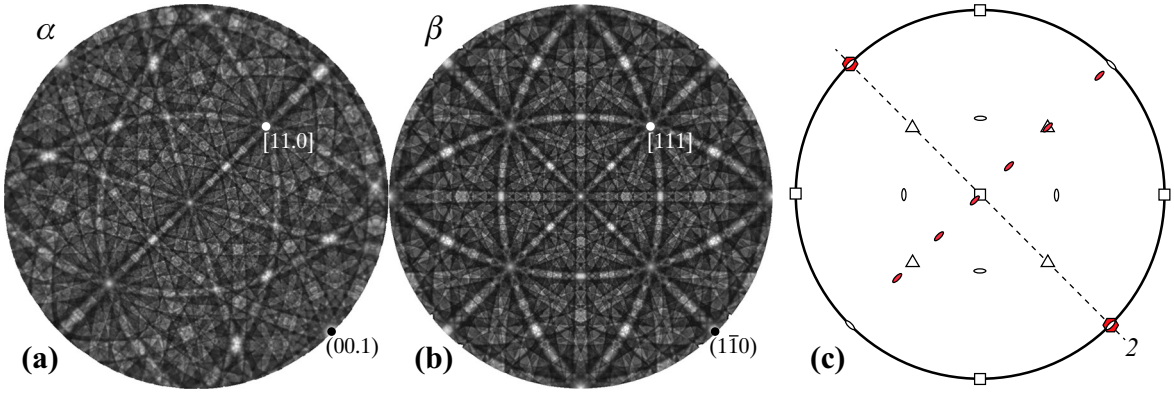

Fig. 3. Stereographic projections of (a) the Lambert master patterns for the α-Ti phase, rotated by the Burgers OR, and (b) the β-Ti phase. In (c), the symmetry elements of each phase are drawn as a stereographic projection (α phase in red, β phase in white).

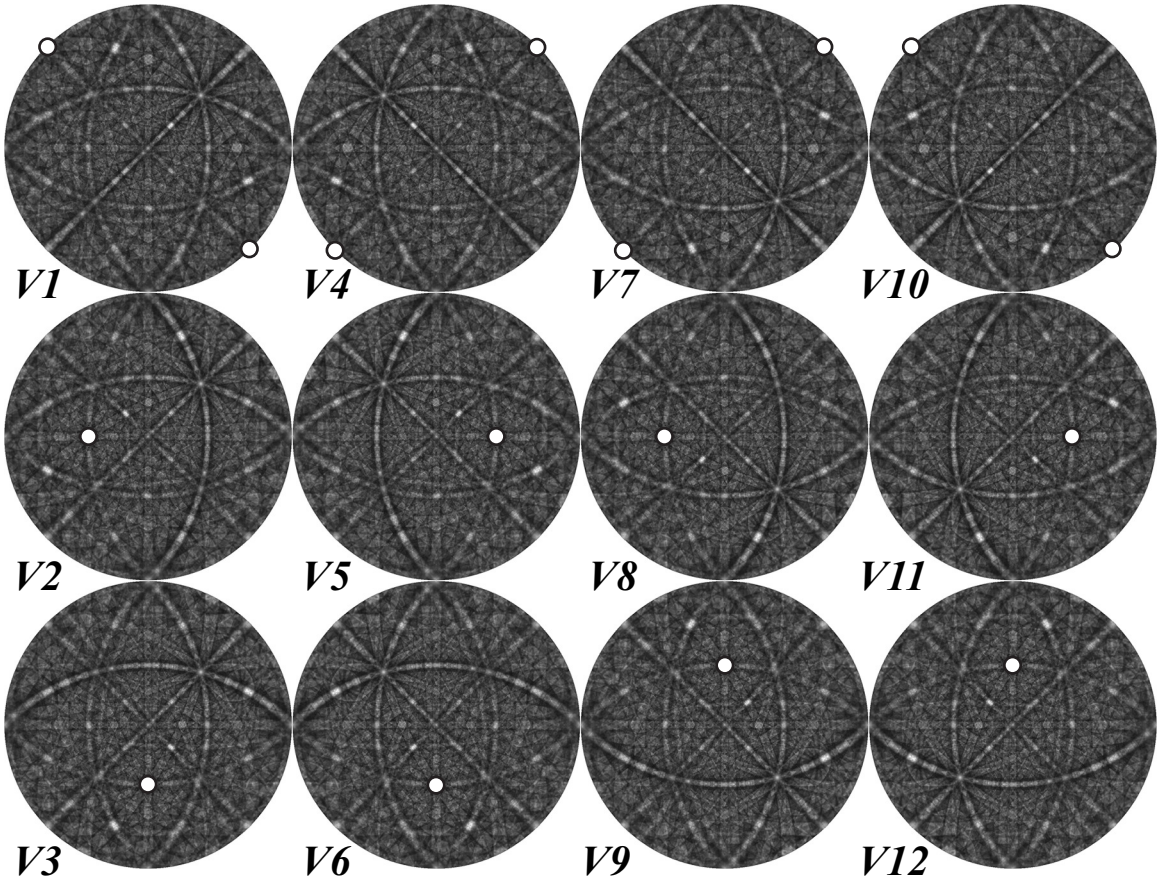

Fig. 4. Stereographic projections of the overlap master patterns for all 12 Burgers orientation variants of the α-Ti phase rotated with respect to a β-Ti phase master pattern. The white circle in each overlap pattern indicates the position of the hexagonal c-axis.

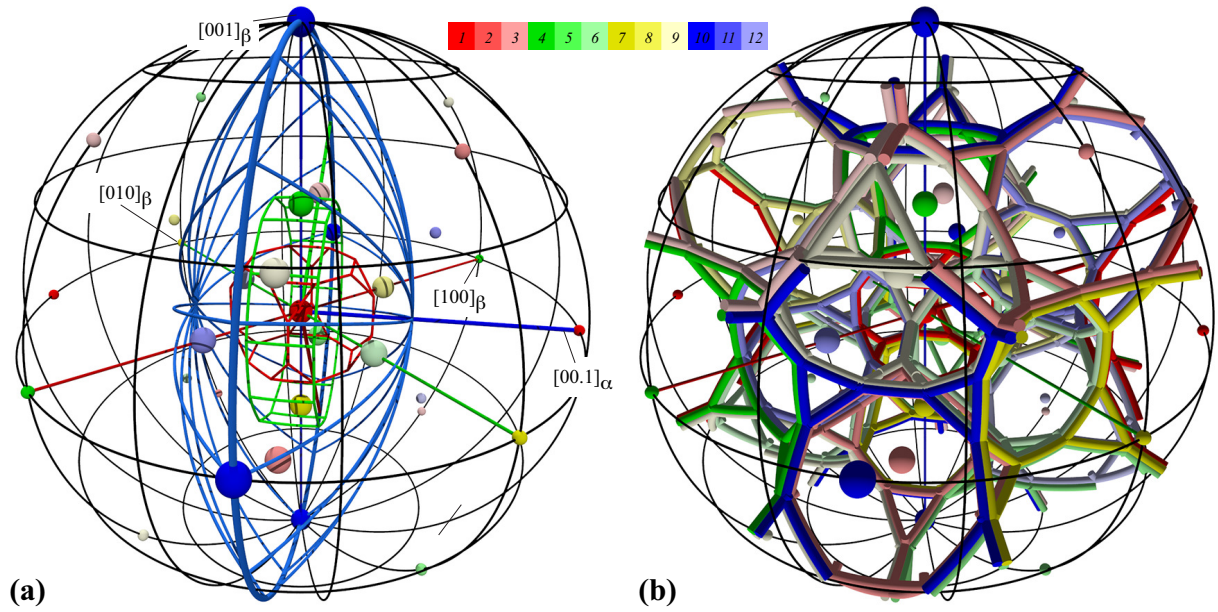

Fig. 5. (a) 3-D stereographic projection showing the cubic (red) and hexagonal (green) fundamental zones in the Burgers OR for variant $V1$, along with the monoclinic fundamental zone outlined in blue as a lens-shaped region. Each of the cubic symmetry operators (expressed as quaternions in Table 2) is represented by a colored sphere; the color corresponds to the α-phase variant as listed in the Table. Variant $V1$ is represented as a sphere in the origin (identity rotation); large spheres indicate equivalent points that fall inside the monoclinic FZ. (b) equivalent cubic fundamental zones drawn as colored wire frames for all of the 12 α variants (two equivalent zones per variant). Animations of both (a) and (b) are available as Supplementary Material.

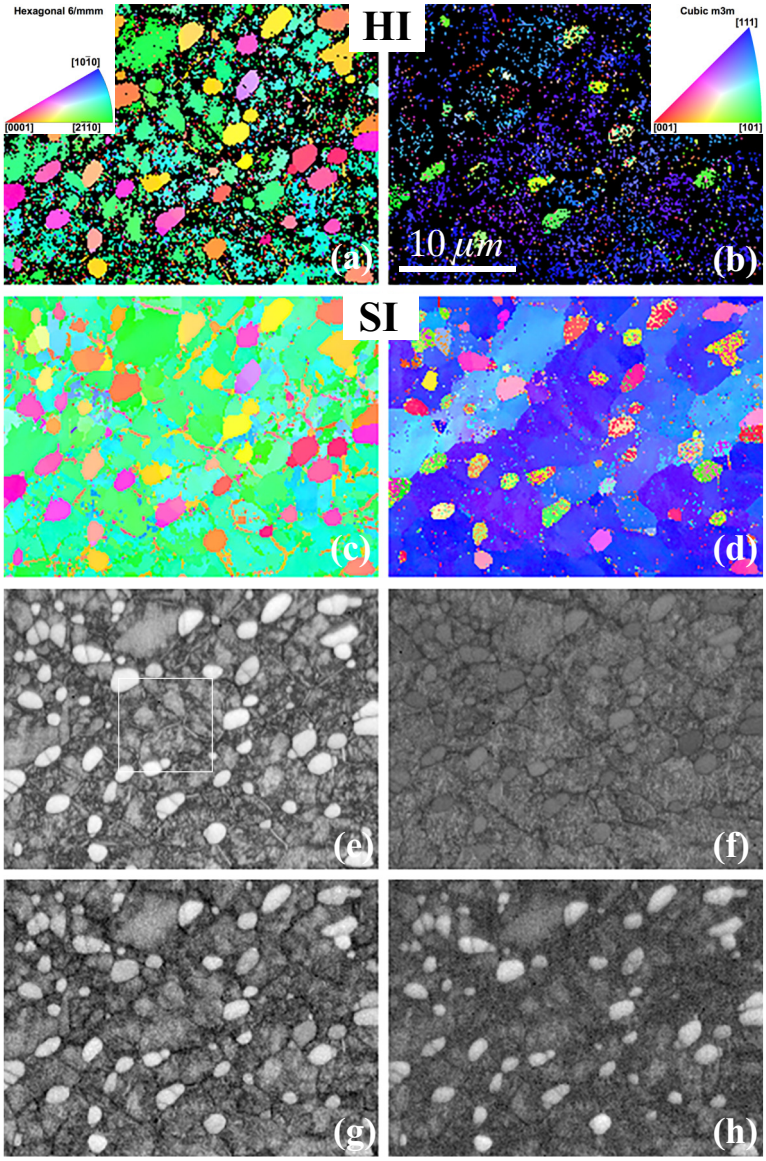

Fig. 6. Hough indexing (a, b) and spherical indexing (c, d) IPF maps for the α (left column) and β (right column) phases for ROI-1. The cross-correlation index maps (e, f) for spherical indexing (i.e., the maximum cross-correlation value) have a range from 0.0 (black) to 0.59 (white). The white rectangle in (e) delineates the second region-of-interest, ROI-2, used in Fig. 7. (g) is the Band Contrast (BC) map as measured by Aztec with an intensity range $[17, 165]$; (h) shows the Image Quality (IQ) map with a range of $[0.093, 0.183]$.

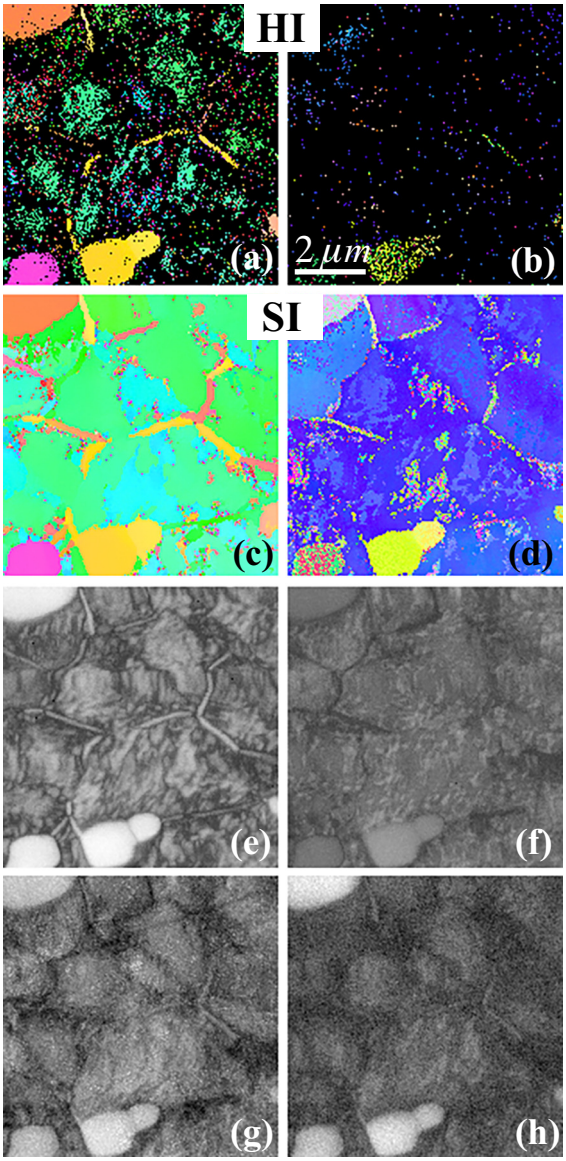

Fig. 7. Hough indexing (a, b) and spherical indexing (c, d) IPF maps for the α (left column) and β (right column) phases for ROI-2. The confidence index maps (e, f) for spherical indexing (i.e., the maximum cross-correlation value) have a range from 0.0 (black) to 0.55 (white). (g) is the Band Contrast (BC) map with an intensity range $[23, 157]$; (h) shows the Image Quality (IQ) map with a range of $[0.055, 0.126]$.

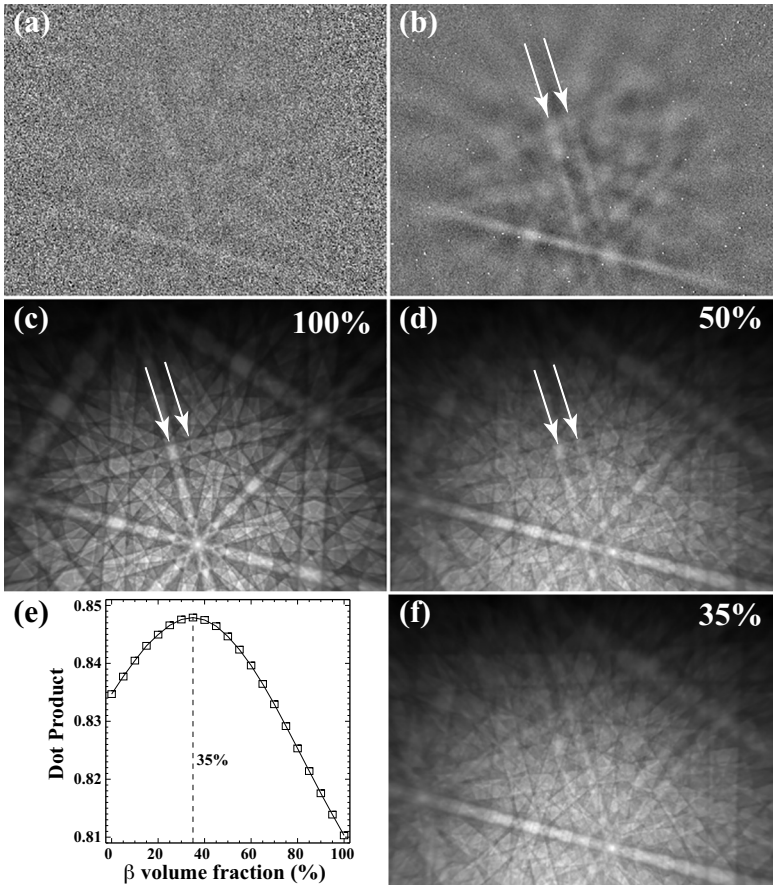

Fig. 8. (a) Experimental background subtracted pattern and (b) averaged pattern over an 11×11 region; (c) simulated pattern for 100% β-phase; (d) 50% β-phase. In (e), the dot product is shown between the pattern in (b) and simulated patterns as a function of the β-phase volume fraction; the simulated pattern corresponding to the maximum at 35% is shown in (f).

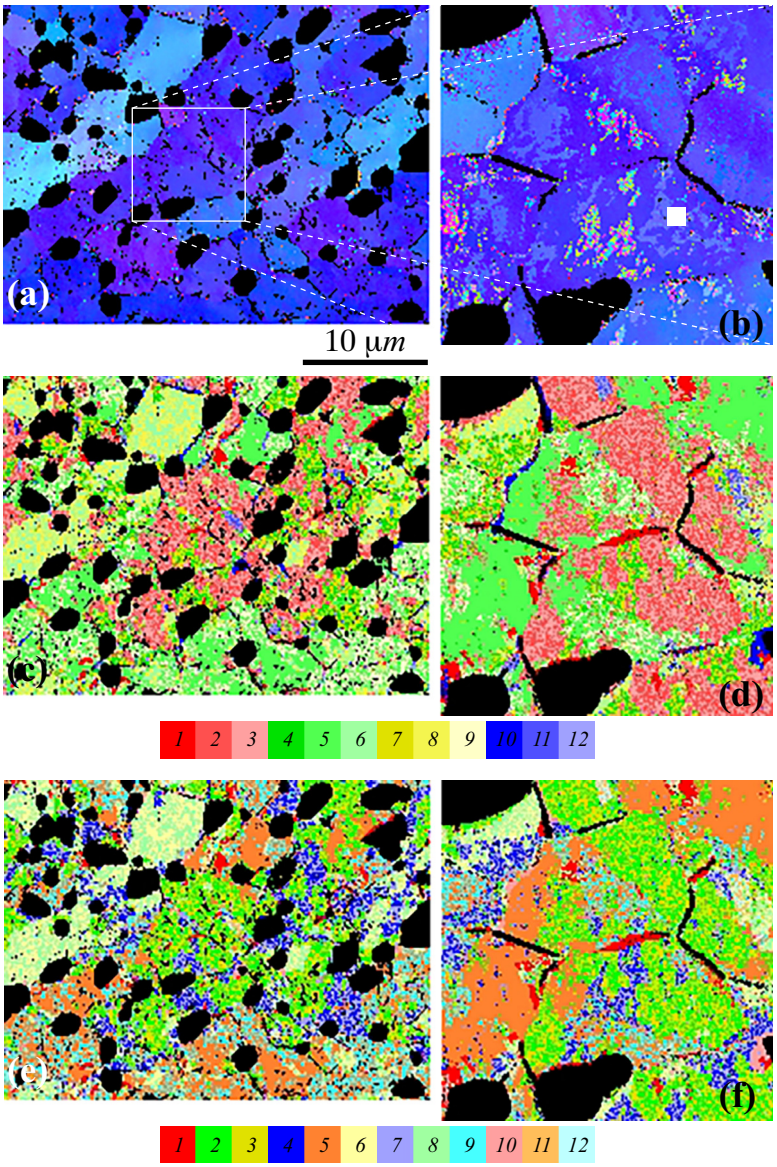

Fig. 9. (a)-(b) IPF-Z maps derived from spherical indexing with the overlap master pattern; all orientations were reduced to the cubic fundamental zone. (c)-(d) α variant map derived from spherical indexing with bandwidth 263 by means of the algorithm explained in the text; the color scheme emphasizes groups of α laths with common $\langle 111 \rangle_\beta$ directions. (e)-(f) same as (e)-(d) but with a color scheme that highlights variants with common $\{110\}_\beta$ planes.

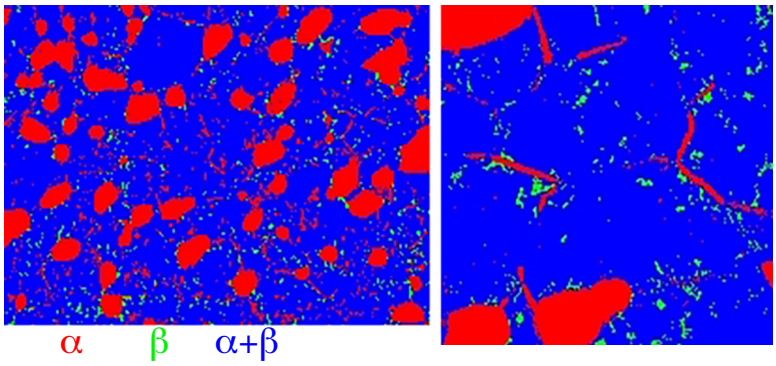

Fig. 10. Phase maps based on the spherical indexing cross-correlation values; red: α-phase, green: β-phase, blue: α+β, indexed with respect to the overlap master pattern.

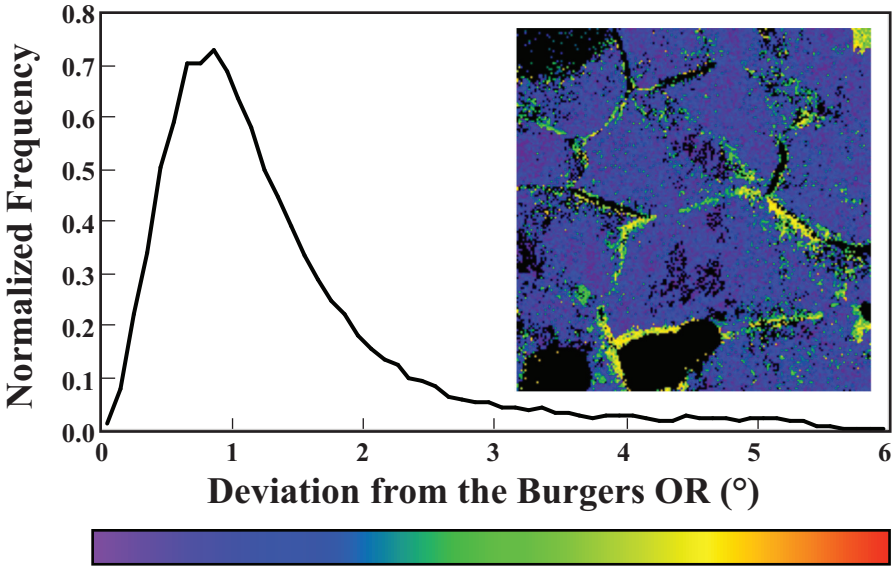

Fig. 11. Deviation angle (in degrees) from the Burgers OR; the tail of the distribution corresponds to the α precipitates that have nucleated at the transformed β boundaries.

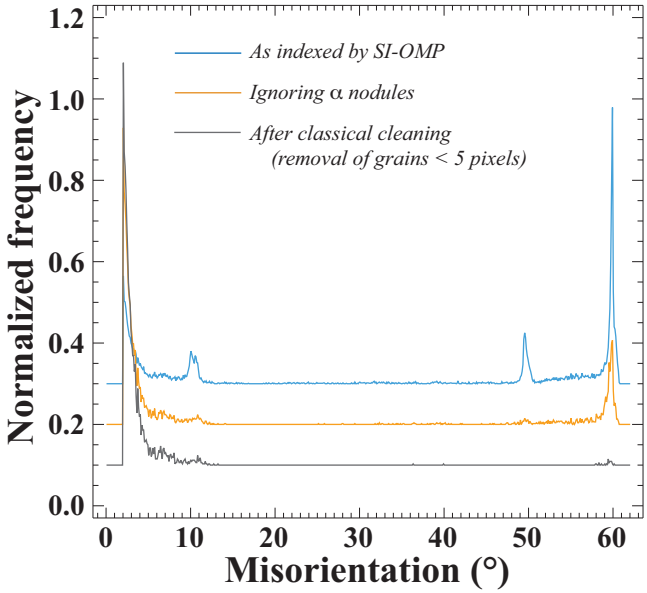

Fig. 12. Misorientation angles distribution for the β bcc phase from ROI-1 indexed with SI-OMP. In blue, results from the raw indexation; in orange, the same as blue but ignoring the α nodules; in gray, after removing all grains having a size under 5 pixels.

A Determination of an OR rotation matrix

We begin by creating two cartesian reference frames, one for each phase, based on the OR vectors $\mathbf{t}^{A,B}$ and $\mathbf{g}^{A,B}$; to avoid confusion between the standard Cartesian reference frame introduced in the previous section, and the two Cartesian reference frames needed for the OR, we will use a different letter $\mathbf{f}$ to indicate the OR Cartesian basis vectors:

$$\begin{aligned}
\mathbf{f}_1^{A,B} &= \frac{\mathbf{g}^{A,B}}{||\mathbf{g}^{A,B}||} \equiv \hat{\mathbf{g}}^{A,B}; \\
\mathbf{f}_2^{A,B} &= \mathbf{f}_3^{A,B} \times \mathbf{f}_1^{A,B}; \\
\mathbf{f}_3^{A,B} &= \frac{\mathbf{t}^{A,B}}{||\mathbf{t}^{A,B}||} \equiv \hat{\mathbf{t}}^{A,B}.
\end{aligned} \tag{A.1}$$

The Cartesian reference frames can then be written in terms of the Bravais lattice basis vectors as:

$$\mathbf{f}_i^{A,B} = E_{ij}^{A,B} \mathbf{a}_j^{A,B},$$

where the $E_{ij}^{A,B}$ are 3×3 matrices. Equating the two Cartesian reference frames, we have:

$$E_{ij}^{A} \mathbf{a}_j^{A} = E_{ij}^{B} \mathbf{a}_j^{B},$$

so that

$$\mathbf{a}_i^{A} = \gamma_{ij} \mathbf{a}_j^{B} \quad \text{with} \quad \gamma_{ij} \equiv (E^{A})_{ik}^{-1} E_{kj}^{B}. \tag{A.2}$$

Since an EBSD master pattern is represented with respect to the cartesian crystallographic reference frame, one must, as a final step, convert equation A.2 to the cartesian frames. The transformation from Bravais to cartesian basis vectors is carried out using the reciprocal structure matrix:

$$\mathbf{e}_i^{A,B} = b_{ij}^{A,B} \mathbf{a}_{ij}^{A,B}. \tag{A.3}$$

Equation A.2 then becomes:

$$(b^{A})_{il}^{-1} \mathbf{e}_l^{A} = \gamma_{ij} (b^{B})_{jk}^{-1} \mathbf{e}_k^{B}; \tag{A.4}$$

multiplying both sides by b_{mi}^{A} and using the fact that $b^{-1} = \tilde{a}$ (with a the direct structure matrix), we obtain:

$$\mathbf{e}_m^{A} = b_{mi}^{A} \gamma_{ij} \tilde{a}_{jk}^{B} \mathbf{e}_k^{B} \equiv \rho_{mk} \mathbf{e}_k^{B}. \tag{A.5}$$

A general orientation relation (OR) between two crystal structures A and B can be expressed by a pair of parallel directions (direct space) and plane normals (reciprocal space):

$$\mathbf{t}^A = [uvw]_A \parallel [uvw]_B = \mathbf{t}^B \quad \text{and} \quad \mathbf{g}^A = (hkl)_A \parallel (hkl)_B = \mathbf{g}^B. \tag{A.6}$$

In addition to these two conditions, the zone equation must be satisfied in both structures:

$$\mathbf{t}^A \cdot \mathbf{g}^A = 0 = \mathbf{t}^B \cdot \mathbf{g}^B.$$

Note that the structures A and B can have different symmetries and unit cell sizes. Well known ORs include the fcc twin relation (e.g., [25]), the hcp-fcc relation (e.g., [26]), and the Nishiyama-Wasserman relation for fcc-bcc interfaces (e.g., [27]). In this paper, we focus on the Burgers OR [28] between bcc β-Ti and hcp α-Ti :

$$\mathbf{t}^\beta = [111] \parallel [11.0] = \mathbf{t}^\alpha \quad \text{and} \quad \mathbf{g}^\beta = (1\bar{1}0) \parallel (00.1) = \mathbf{g}^\alpha. \tag{A.7}$$

Crystallographic quantities can be translated from one crystal reference frame to the other by means of a transformation matrix, ρ_{mk}, which can be derived by first restating the OR in terms of Cartesian reference frames for each structure, equating the two reference frames, and finally extracting the transformation matrix; this is an essential step in the creation of an overlap master pattern, and details can be found in Appendix A. To create the master pattern that contains both the Ti-β and Ti-α patterns in the correct OR, we sample the α master pattern at the grid points of the β master pattern, in such a way that the Burgers OR is satisfied. Applying the relations from Appendix A to the Burgers OR (eq. A.7), we obtain after some algebra:

$$\rho_{mk} = \begin{pmatrix} \sqrt{\frac{5}{24} + \frac{1}{2\sqrt{6}}} & \sqrt{\frac{5}{24} + \frac{1}{2\sqrt{6}}} & \frac{1}{2\sqrt{3}} - \frac{1}{\sqrt{2}} \\ \frac{1}{2} - \frac{1}{2\sqrt{6}} & \frac{1}{2} - \frac{1}{2\sqrt{6}} & \frac{1}{2} + \frac{1}{\sqrt{6}} \\ \frac{1}{\sqrt{2}} & -\frac{1}{\sqrt{2}} & 0 \end{pmatrix} = \begin{pmatrix} 0.642229 & 0.642229 & -0.418432 \\ 0.295876 & 0.295876 & 0.908248 \\ 0.707107 & -0.707107 & 0. \end{pmatrix}. \tag{A.8}$$

The corresponding unit quaternion is given by

$$q_\rho = [0.696079, -0.580162, -0.404242, -0.124394], \tag{A.9}$$

with the scalar part as the first entry. We employ mostly quaternion arithmetic in this paper.

B Modified Square Lambert mappings

The equal-area mappings between a regular square, the circular disk and the hemisphere can be carried out by means of the relations described below. Consider a square of edge length $2L$, and a disk of radius R, such that both have the same surface area, i.e., $4L^2 = \pi R^2$. Setting the radius r of the hemisphere to 1, an equal-area mapping between square, disk, and hemisphere can be obtained by equating all surface areas, so that $R = \sqrt{2}$, and $L = \sqrt{\pi/2}$. We represent the coordinates in the square by (a, b), (X, Y) for the circular disk, and (x, y, z) for the hemisphere of radius $r = 1$.

The equal-area Lambert mapping between the disk and the (Northern) hemisphere is given by:

$$(X, Y) = \sqrt{\frac{2}{1-z}}(x, y); \tag{B.1}$$

$$(x, y, z) = \left(\sqrt{1 - \frac{X^2+Y^2}{4}}X, \sqrt{1 - \frac{X^2+Y^2}{4}}X, 1 + \frac{X^2+Y^2}{2}\right). \tag{B.2}$$

The transformation relations between the square and the hemisphere are given by [13]:

$$(x, y, z) = \left(\frac{2a}{\pi}\sqrt{\pi - a^2}\cos\frac{b\pi}{4a}, \frac{2a}{\pi}\sqrt{\pi - a^2}\sin\frac{b\pi}{4a}, \frac{2a^2}{\pi} - 1\right) \quad 0 < |b| \le |a| \le L; \tag{B.3}$$

$$(x, y, z) = \left(\frac{2b}{\pi}\sqrt{\pi - b^2}\sin\frac{a\pi}{4b}, \frac{2b}{\pi}\sqrt{\pi - b^2}\cos\frac{a\pi}{4b}, \frac{2b^2}{\pi} - 1\right) \quad 0 < |a| \le |b| \le L, \tag{B.4}$$

and

$$(a, b) = \text{sign}(x)\sqrt{2(1-z)}\left(\frac{\sqrt{\pi}}{2}, \frac{2}{\sqrt{\pi}}\arctan\frac{y}{x}\right) \quad 0 \le |y| \le |x|; \tag{B.5}$$

$$(a, b) = \text{sign}(y)\sqrt{2(1-z)}\left(\frac{2}{\sqrt{\pi}}\arctan\frac{x}{y}, \frac{\sqrt{\pi}}{2}\right) \quad 0 \le |x| \le |y|. \tag{B.6}$$

The transformation relations are represented in short hand notation as

$$(a, b) = \mathcal{L}[x, y, z] \quad \text{and} \quad (x, y, z) = \mathcal{L}^{-1}[a, b]. \tag{B.7}$$

C Group theoretical analysis of the α variants

The cubic β-phase symmetry is described by the rotational point group $\mathcal{G} = \mathbf{432}$ (since we are only concerned with orientations, we omit mirror planes and the inversion from the point group descriptions). In this section, the rotational overlap master pattern symmetry is represented by the sub-group $\mathcal{H} \subset \mathcal{G}$ which equals the monoclinic group **2** for the Burgers OR. The number of variants for the orientation relation is given by the ratio of the rotational point group orders, $N_v \equiv N_{\mathcal{G}}/N_{\mathcal{H}}$, which reduces to the expected $N_v = 24/2 = 12$ for the Burgers OR. The rotational cubic group can be written in a co-set decomposition with respect to the group $\mathcal{H}$ as the sum of two sets, namely $\mathcal{G} = \mathcal{B} + 2_{1\bar{1}0}\mathcal{B}$ where $2_{1\bar{1}0}$ is the monoclinic two-fold rotation axis around $[1\bar{1}0]_\beta$, and $\mathcal{B}$ is the set that produces all the α-phase orientations starting from variant V_1 (i.e., $\mathcal{B} = \{q_{Vj}\}$ referring to Table 2). Thus, for every element $q_{Vj} \in \mathcal{B}$ there is a second rotation, $2_{1\bar{1}0}q_{Vj}$, that generates the same variant; only one of these two equivalent rotations falls inside the monoclinic fundamental zone. For a given q_β, application of all elements of $\mathcal{B}$ generates 11 new orientations that represent the different α orientation variants; in other words, $q_{Vj}q_\beta$ generates equivalent β orientations, but each with a different associated α variant.